




Article

Degradation Kinetics of Methyl Orange Dye in Water Using Trimetallic Fe/Cu/Ag Nanoparticles

Masaku Kgatle ^{1,2}, Keneiloe Sikhwivhilu ^{1,*}, Gebhu Ndlovu ¹ and Nosipho Moloto ²

¹ DSI/Mintek Nanotechnology Innovation Centre, Advanced Materials Division, Mintek, Private Bag X3015, Randburg 2125, South Africa; kmasaku@yahoo.com (M.K.); GebhuN@mintek.co.za (G.N.)

² Molecular Sciences Institute, School of Chemistry, University of the Witwatersrand, Private Bag 3, Johannesburg 2050, South Africa; Nosipho.Moloto@wits.ac.za

* Correspondence: Keneiloes@mintek.co.za

Abstract: The release of azo dye contaminants from textile industries into the environment is an issue of major concern. Nanoscale zerovalent iron (nZVI) has been extensively studied in the degradation of azo dye pollutants such as methyl orange (MO). In this study, iron was coupled with copper and silver to make trimetallic Fe/Cu/Ag nanoparticles, in order to enhance the degradation of MO and increase reactivity of the catalyst by delaying the rate of oxidation of iron. The synthesis of the trimetallic nanoparticles (Fe/Cu/Ag) was carried out using the sodium borohydride reduction method. The characterization of the particles was performed using XRD, XPS, EDX, and TEM. The analyses confirmed the successful synthesis of the nanoparticles; the TEM images also showed the desired structures and geometry of the nanoscale zerovalent iron particles. The assessment of the nanoparticles in the degradation of methyl orange showed a notable degradation within few minutes into the reaction. The effect of parameters such as nanoparticle dosage, initial MO concentration, and the solution pH on the degradation of MO using the nanoparticles was investigated. Methyl orange degradation efficiency reached 100% within 1 min into the reaction at a low pH, with lower initial MO concentration and higher nanoparticle dosage. The degradation rate of MO using the nanoparticles followed pseudo first-order kinetics and was greatly influenced by the studied parameters. Additionally, LC-MS technique confirmed the degradation of MO within 1 min and that the degradation occurs through the splitting of the azo bond. The Fe/Cu/Ag trimetallic nanoparticles have proven to be an appropriate and efficient alternative for the treatment of dye wastewater.

Keywords: trimetallic catalysts; methyl orange; nanoscale zerovalent iron; Fe/Cu/Ag nanoparticles



Citation: Kgatle, M.; Sikhwivhilu, K.; Ndlovu, G.; Moloto, N. Degradation Kinetics of Methyl Orange Dye in Water Using Trimetallic Fe/Cu/Ag Nanoparticles. *Catalysts* **2021**, *11*, 428.

<https://doi.org/10.3390/catal11040428>

Academic Editors: Vincenzo Vaiano and Olga Sacco

Received: 5 February 2021

Accepted: 6 March 2021

Published: 26 March 2021

Publisher's Note: MDPI stays neutral with regard to jurisdictional claims in published maps and institutional affiliations.



Copyright: © 2021 by the authors. Licensee MDPI, Basel, Switzerland. This article is an open access article distributed under the terms and conditions of the Creative Commons Attribution (CC BY) license (<https://creativecommons.org/licenses/by/4.0/>).

1. Introduction

The deterioration in the quality of water is one of the key factors of water risks and this has drawn researchers' attention to alleviating the issue [1,2]. The discharge of untreated effluent from industries such as leather, textile, ink, cosmetics, and paper into the water streams turns out to be a serious threat to living beings [3,4]. As such, dyeing industries are regarded as one of the world's largest water polluters as their effluent is made up of toxic compounds; dyes are carcinogenic in nature and refractory to biodegradation [2]. Among the 10,000 distinctive dyes and colorants used in the textile industry, above 50% are azo dyes [5]. Azo dyes are distinguished by the presence of the azo bond (–N=N–) which in turn influences the bright color of their aqueous solutions [6]. Due to their qualities, such as being water soluble, possessing a complicated structure, and being of synthetic origin; removal of azo dyes is generally challenging [7,8].

In order to remove dyes from wastewater; physical, chemical, and biological methods such as adsorption, chlorination, coagulation, ozonation, and membrane filtration have been used [5,7]. However, some of these techniques do not lead to the degradation of the dye, but simply physically remove the dye component from the effluent, thereby maintaining the waste removal issue [5]. Moreover, other techniques lead to secondary

pollution, elevating the problem of pollution [5]. Much consideration has been given into developing new treatment approaches to eliminate dyes from the environment. Nanoscale zerovalent iron (nZVI) has since materialized as an effective solution for the remediation of dye wastewater because of its low-cost, great reduction capabilities and the capacity to degrade pollutants [2,9–11]. In the degradation of toxic dye molecules, nZVI particles are oxidized, thereby donating two electrons to the dye molecule leading to its reduction [2,12]. Nonetheless, the use of nZVI for the elimination of pollutants has some inherent constraints such as the progressive decline in reactivity owing to surface passivation induced by the corrosion of nZVI [13,14]. To overcome the aforementioned drawback of nZVI technology, numerous solutions have been created; and the one that has gained momentum over the years is depositing a second metal which serves as a catalyst on the iron surface [15].

The benefits of bimetallic nanoparticles are: greater surface area and density of reactive sites and hindrance of the corrosion products from accumulating on ZVI reactive surface sites [16]. Essentially, partial coverage of nZVI by metals such as Pd [17], Pt [18], Ni [16], Cu [19], or Ag [20] leads to increased effectiveness of nZVI in multiple applications. The aforementioned catalytic metals reinforce the production of atomic hydrogen or hydride on the surface in all iron-based bimetallic systems and alter the electronic characteristics of nZVI, the electron donor and reducing agent [16]. Moreover, bimetallic particle reduction rates are considerably quicker than those for nZVI alone, and they have greater stability for degradation and avoidance, or lessening of the creation and build-up of toxic by-products [21]. Due to the creation of an iron hydroxide layer which may delay interaction of the reactant with the catalyst, the effectiveness of the catalyst used in the bimetallic nanoparticle scheme decreases over time [22]. Consequently, although bimetallic particles show increased reduction rates, trimetallic materials were studied accordingly and showed better efficiency than bimetallic materials [14].

The aim of this research study was to synthesize and characterize Fe/Cu/Ag trimetallic nanoparticles for the degradation of methyl orange dye in wastewater. While some metal catalysts (i.e., Pt, Pd and Au) have satisfactory outcomes in laboratory-scale research for the Fe-based bimetallic [17] and trimetallic [23], these are overly expensive to use in wastewater remediation applications. Hence the need to attain a cost-effective and greatly reactive nZVI-based trimetallic system with minimal mass loading and low-cost metal catalysts.

2. Results and Discussion

2.1. Material Characterization

The X-ray diffraction (XRD) patterns of nZVI (Fe^0), Fe/Ag (5:0.1), Fe/Cu (5:1) and Fe/Cu/Ag (5:1:0.2) nanoparticles and standard reference patterns of the metals and oxides are summarized in Figure 1. The presence of zero-valent iron (Fe^0) in all the XRD spectra is marked by the reflections appearing at 2θ values of $46\text{--}47^\circ$ representing the body centered cubic (bcc) lattice plane (110). The massive presence of Fe_2O_3 peaks in the spectra suggests that iron is extremely prone to oxidation [24]. The Fe/Ag diffractogram shows a diffraction peak largely associated with the cubic Ag at 39.5° corresponding to the (111) lattice plane. On the other hand, the Fe/Cu pattern has a minor peak at the 2θ value of 53.5° , corresponding to the (200) crystalline plane; which is assigned to a cubic phase of Cu. The trimetallic particles Fe/Cu/Ag diffraction pattern is indexed mainly to Fe^0 , similar to the other patterns; with the additional peaks of both Cu and Ag as observed in the bimetallic nanoparticles' XRD patterns. Copper is also readily oxidized, however no significant peaks of CuO were observed in any copper-containing particles. The average crystallite sizes for the nZVI, Fe/Ag, Fe/Cu, and Fe/Cu/Ag nanoparticles, as determined using the Scherrer equation from the most intense common peak ($36^\circ 2\theta$), are 18.9, 27.3, 14.7, and 11.4 nm, respectively. The trimetallic crystallite sizes are smaller than the nZVI and the bimetallic nanoparticles, suggesting a decrease in the average crystallite diameters of Ag and Cu in the trimetallic system [25]. The study carried out by Mahmoud et al. [26] established that the nZVI crystallite sizes were greater than those of the bimetallic Fe/Cu because the magnetic forces between nZVI particles lead to the creation of larger nan-

oclusters. On the other hand, the copper on the bimetallic Fe/Cu nanoparticles impedes magnetic forces between nZVI nanoparticles, thereby leading to smaller nanoclusters [26]; hence, the smaller crystallite sizes observed for the bimetallic and trimetallic nanoparticles in comparison to the nZVI as reported herein. Moreover, Al-Namil et al. [27] have shown that smaller crystallite sizes have greater catalytic activity for the reduction studies.

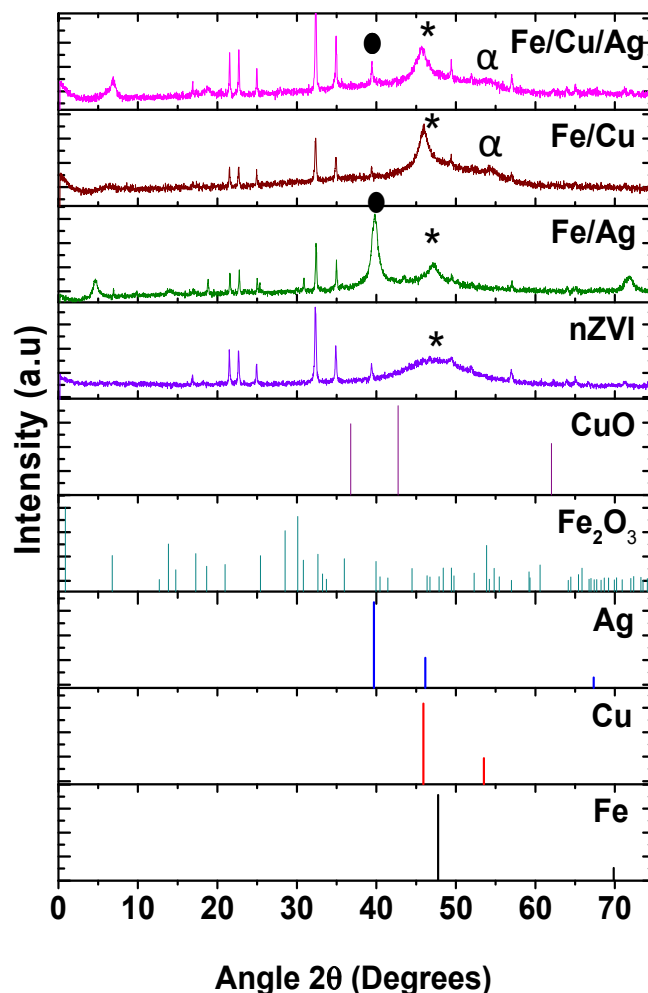


Figure 1. XRD patterns of nZVI, Fe/Ag (5:0.1), Fe/Cu (5:1) and Fe/Cu/Ag (5:1:0.2) nanoparticles and the relevant standard reference patterns. (* Peaks of Fe⁰, α Peaks of metallic Cu and ● Peaks of metallic Ag).

Figure 2 presents the EDX data analysis of the nZVI (Fe⁰) and Fe/Cu/Ag nanoparticles. The EDX spectrum of nZVI (Fe⁰) shows a peak for Fe at 6–7 keV and O at 0.6 keV which is due to the formation of iron oxide as observed in the XRD pattern. The EDX spectrum of Fe/Cu/Ag specifies the presence of metallic Fe, Ag, and Cu at 6–7, 2.5–3, and 1 keV, respectively. The presence of the oxygen peak in the EDX spectra substantiated the oxidation of Fe into corresponding oxides as shown in the XRD pattern. Additionally, the carbon is due to the surfactant, PVP, while the nickel comes from nickel grids.

Additional characterization of the nanoparticles was conducted using XPS analysis, which is an effective surface-sensitive analytical technique used to determine elemental composition. The XPS survey and high-resolution spectra of each sample were measured and the latter was used for thorough chemical analysis, these are shown in Figure 3 while the XPS survey spectra are also detailed in the Appendix A (Figure A1). The nZVI (Fe⁰) survey spectrum shows the presence of C, O, and Fe. The C is attributed to the surfactant used (i.e., PVP) and the O emanates from Fe₂O₃ that was observed in the XRD results.

All the survey spectra show C and O while Fe/Ag and Fe/Cu show Fe, Ag, and Cu. The atomic composition of each element present is summarized in Table 1. In all samples, there is a high percentage of C and O. The C as previously stated, is attributed to the PVP surfactant used in the synthesis. The O is attributed to Fe₂O₃ and this is consistent with the XRD data. All samples also show the presence of Fe, which was also observed in the XRD spectra. The Fe/Ag and Fe/Cu samples show a higher atomic % of Fe as compared to Ag and Cu. This is consistent with the ratios used. In Fe/Cu/Ag, the amount of Cu is slightly higher than that of Fe, which is somewhat unexpected.

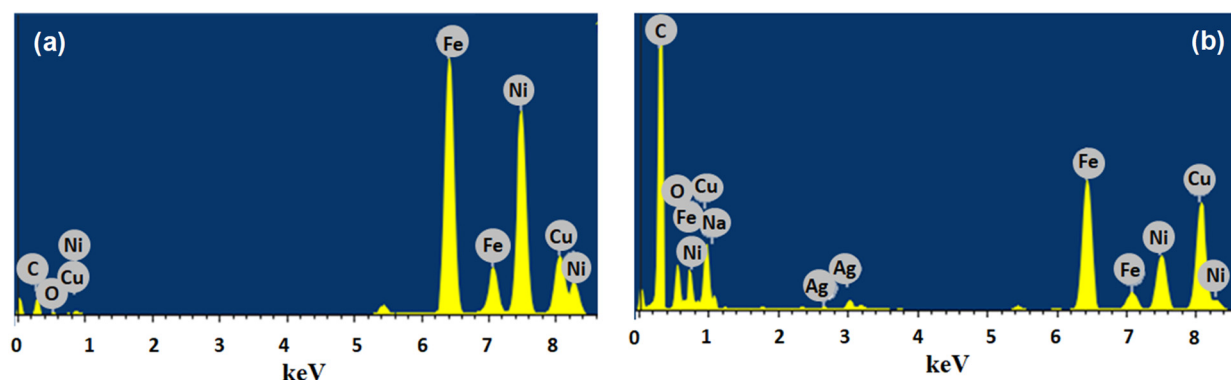


Figure 2. The EDX spectra of (a) nZVI (Fe⁰) nanoparticles and (b) Fe/Cu/Ag (5:1:0.2).

Table 1. Atomic composition extracted from the XPS of nZVI (Fe⁰), Fe/Ag (5:0.1), Fe/Cu (5:1) and Fe/Cu/Ag (5:1:0.2) nanoparticles.

Sample	Element	Peak Binding Energy (eV)	Atomic %
nZVI (Fe ⁰)	C	288.4	41.75
	O	529.6	53.59
	Fe	713.9	3.47
Fe/Ag	C	287.9	40.96
	O	528.6	51.42
	Fe	713.6	6.20
	Ag	371.07	1.42
Fe/Cu	C	288.4	41.99
	O	533.6	59.96
	Fe	713.9	3.32
	Cu	940.9	2.73
Fe/Cu/Ag	C	283.6	50.5
	O	533.6	45.58
	Fe	713.6	1.68
	Ag	376.3	0.22
	Cu	936.3	2.02

The high-resolution Fe 2p spectrum of nZVI (Fe⁰) displays four peaks corresponding to Fe⁰ (720.0 and 706.3 eV), Fe₂O₃ (Fe 2p_{3/2} (710.4 eV)), and Fe₂O₃ (Fe 2p_{1/2} (724 eV)) [28–30]. The Fe 2p for the bimetallic Fe/Ag and Fe/Cu as well as the trimetallic Fe/Cu/Ag were identical. The XPS spectra shows the presence of metallic Fe, as observed in the XRD patterns. Since XRD is a bulk technique, the overwhelming amount of Fe₂O₃ masks some of the species that might be present.

The high-resolution Ag 3d spectra for Fe/Ag and Fe/Cu/Ag nanoparticles show two peaks at 367.3 eV (Ag 3d_{5/2}) and 374.2 eV (Ag 3d_{3/2}), corresponding to metallic silver [31]. Furthermore, the Cu 2p high-resolution spectra of Fe/Cu and Fe/Cu/Ag show peaks at 932.1 eV and 953.3 eV corresponding to Cu 2p_{3/2} and Cu 2p_{1/2}, respectively, which correlate to metallic copper [31]. In addition to this, there are Cu²⁺ peaks associated with copper oxide. There was no overwhelming evidence of CuO in the XRD patterns [28,30,32].

This suggests that the oxidation of copper is only surface deep. Most significantly, these results confirm the successful synthesis of the trimetallic nanoparticles.

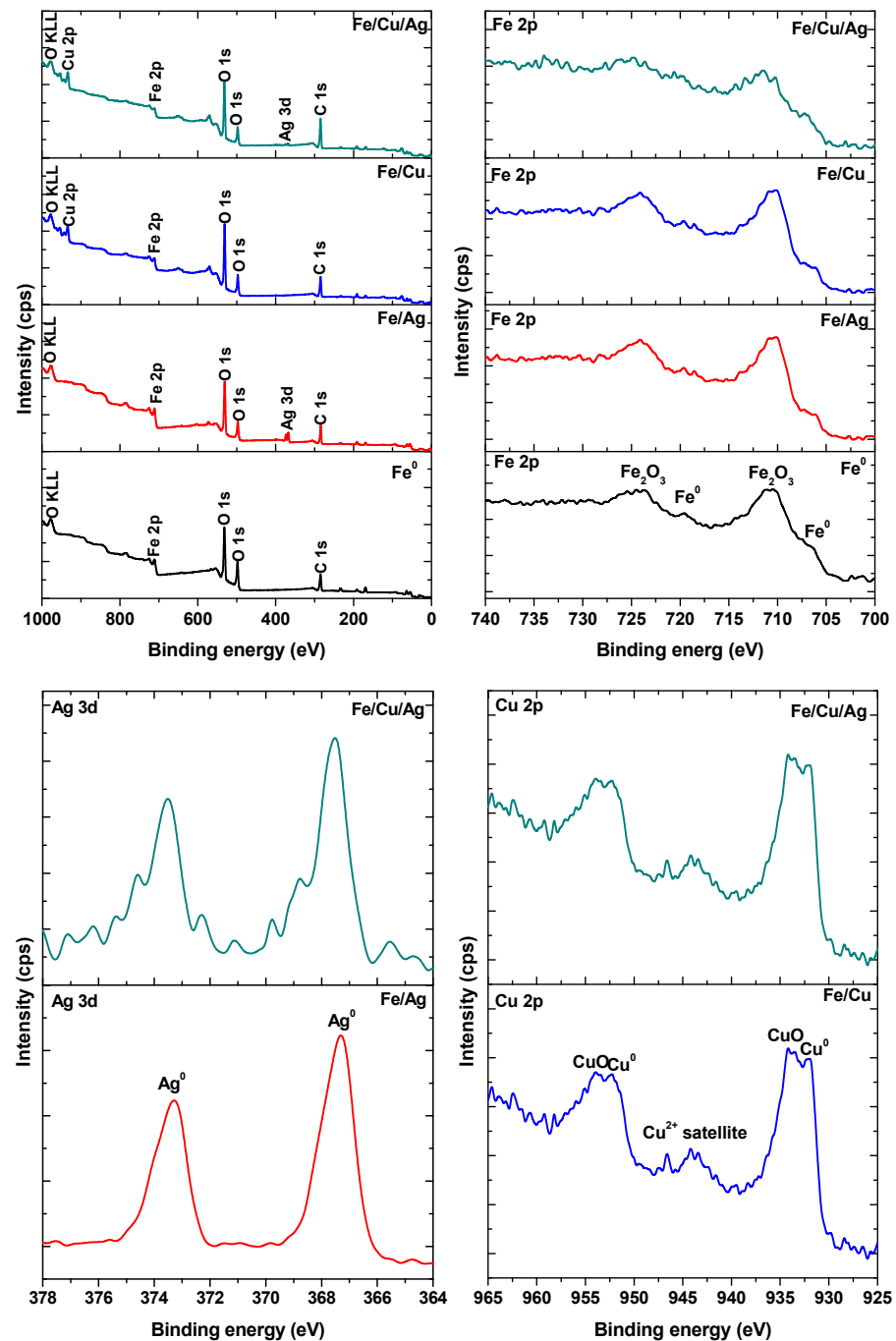


Figure 3. XPS survey spectra, Fe 2p, Ag 3d and Cu 2p high-resolution spectra of nZVI (Fe⁰), Fe/Cu (5:1), Fe/Ag (5:0.1), and Fe/Cu/Ag (5:1:0.2) nanoparticles.

Figure 4 displays the typical TEM micrographs of all the fabricated nanoparticles. Both the nZVI(Fe⁰) and Fe-composite nanoparticles are nearly spherical in shape and appear as noticeable chain-like agglomerates due to the enormous energy interface and magnetic properties of Fe particles [33]. The nanoparticles all show a contrast between the core and the shell, which is the same as the Fe/Cu bimetallic nanoparticles reported by Wang et al. [30] and Fe/Ag bimetallic nanoparticles reported by Luo et al. [34]. From the nanoparticle preparation method, the core is comprised of metallic iron and the shell

consists of iron oxide coexisting with Ag, Cu, or both depending on the composition of the particles. According to the histograms, the particle sizes for nZVI, Fe/Ag, Fe/Cu, and Fe/Cu/Ag nanoparticles range from 40–60, 40–70, 40–70, and 60–90 nm, respectively. It has been established that the particle size calculated by TEM is higher than the crystal-lite size calculated by XRD [35]. This is because one particle can be composed of multiple crystalline domains, which is why particle size is nearly always larger than crystallite size [36].

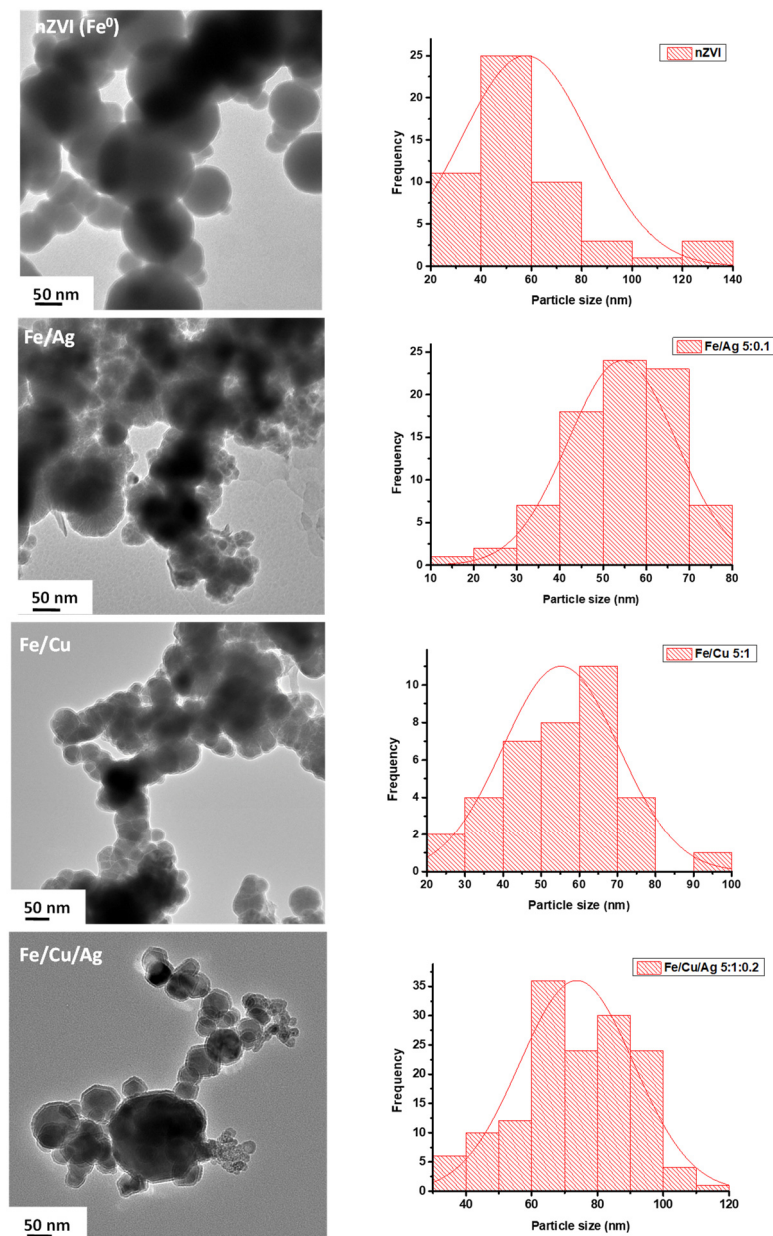


Figure 4. TEM images of nZVI, Fe/Ag 5:0.1, Fe/Cu 5:1, Fe/Cu/Ag 5:1:0.2 and the corresponding particle size histograms.

2.2. Performance of the Nanoparticles in Methyl Orange Degradation

2.2.1. Effect of Catalyst on the Degradation of MO Dye

The degradation of 10 mg/L MO dye was performed at room temperature using unsupported nanoparticles at an unmodified MO dye pH of ~4.5; this was also performed to optimize the degradation of MO using trimetallic nanoparticles. It was observed that the color of the MO dye fades away as the degradation occurs within just a few minutes

of stirring the MO solution in the presence of nanoparticles. The UV absorption spectra of the MO dye solution (presented in Figure A2) showed a gradual decrease in the height of the absorption band for MO at the wavelength of 464 nm over time; displaying the decline in MO dye concentration in the solution. In Figure 5, it is observed that MO dye degradation by the nanoparticles occurs rapidly. Figure 5 also showed that the degradation efficiency of the Fe/Cu bimetallic system was higher than that of nZVI as expected and the same observation was reported by Bransfield et al. [23]. The addition of Cu on the surface of nZVI improved the degradation because of the synergistic effect between Cu and Fe, which enhances the catalytic activity of the Fe/Cu system and also the degradation capabilities [19,37]. The effective degradation of organic pollutants using Fe/Cu nanoparticles, which are cost-effective, has also been reported by various researchers [21,30,38]. The degradation efficiency of Fe/Ag 5:0.1 was lower than that of nZVI. According to Luo et al. [34], the performance of Fe/Ag nanoparticles is slower than of nZVI unless the reaction is enhanced by ultrasonic radiation. Thus, the study showed that in the absence of ultrasonic radiation, the reaction of Fe/Ag firstly proceeds via adsorption of the dye and thereafter, Fe dissolves due to weakly acidic conditions, thereby releasing the adsorbed dye molecules from the surface of the nanoparticles, leading to a decline in degradation efficiency. Additionally, the degradation efficiencies obtained with the Fe/Cu/Ag trimetallic systems were greater than those attained with Fe/Cu, Fe/Ag, and nZVI. The degradation efficiencies of the trimetallic nanoparticles did not increase with an increase in Ag content as one would expect. This is attributed to the fact that at a certain point of increasing the Ag content, the degradation efficiency is negatively influenced after reaching the critical point [34]; in this case 5:1:0.2 was the optimum ratio for MO dye degradation using the trimetallic Fe/Cu/Ag nanoparticles. According to Luo et al. [34], increasing the content of Ag beyond a certain threshold could impede the production of H₂ by the corrosion of iron.

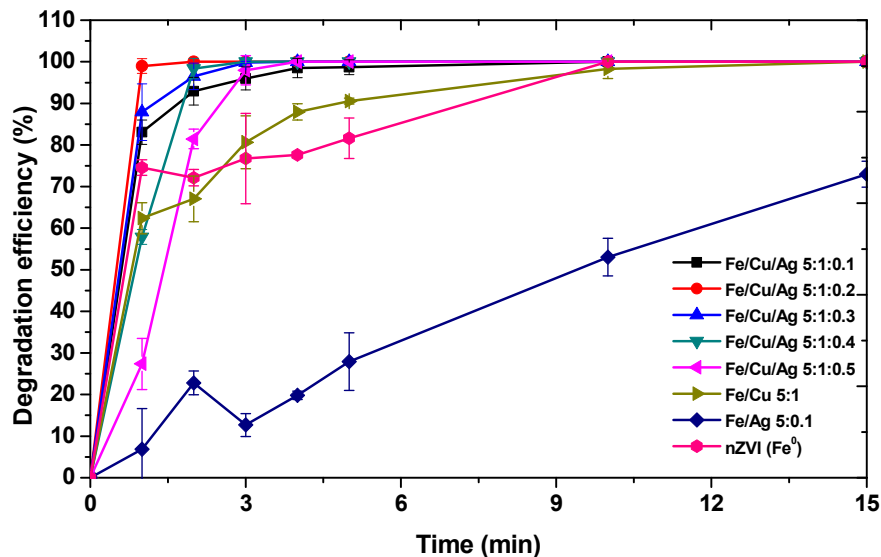


Figure 5. Effect of catalyst composition on MO (pH = ~4.5) degradation efficiency.

The catalytic activity of bimetallic and trimetallic nanoparticles has also been related to properties of individual metals such as electron configuration, electronegativity, and reduction potential. It has been demonstrated that the elements in group 8 and 11 of the periodic table have excellent catalytic properties owing to configuration fluctuations [39,40]. Furthermore, transition metals with unfilled d-shells, and thus presence of unpaired electrons, are more catalytically active [41]. In this case, both Cu and Ag are in group 11 of the periodic table, although they have filled d-electron shells, they are easily excited to sp-states and catalytic activity is produced by the consequent unpaired d-electrons [41]. In addition, the electronegativity of Fe (1.83) is lower than those of Cu (1.90) and Ag (1.93); as a result, it is easier for Fe which has the lowest electronegativity to transfer electrons to

Cu then Ag [42]. This can also be explained by the standard reduction potential trend of the metals: Fe ($E^0 = -0.447$ V) < Cu ($E^0 = 0.34$ V) < Ag ($E^0 = 0.80$ V). It has been shown that the increasing trend in the reduction potential of the metals on Fe core enhances the catalytic activity of the metals [14,43]. This is because the corrosion of Fe releases electrons that progressively travel to the Cu layer and then the Ag layer due to the increase in reduction potential; leading to a high electron density at the Ag layer which can promote the generation of H₂ and enhance the reactivity of Fe/Cu/Ag 5:1:0.2 nanoparticles [14].

Additionally, it has been stated that the addition of lesser amounts of the second and third metals on iron will lead to lesser agglomeration of the synthesized nanoparticles [44]. The Fe/Cu/Ag 5:1:0.2 trimetallic nanoparticles are suitable for the degradation of MO in aqueous solution as the degradation occurs rapidly; the metals are not too costly in comparison with certain metals used in the presence of iron (e.g., Pd and Pt) [45,46], and there is a major delay in the formation of oxides that will hinder the degradation of MO. The addition of Cu and Ag has the capability to stimulate the corrosion of iron, accelerate hydrogen evolution, and produce and retain adsorbed atomic hydrogen on the surface of the particle [34]. Moreover, like Fe, Cu also plays a critical role in the reduction of organic dyes [47,48] and might also be directly involved in the reduction of MO in this instance.

The comparison of surface area characteristics of the catalysts and their efficiency in the degradation of MO dye, the latter measured by turnover number (TON) and turnover frequency (TOF), was done and the results are summarized in Table 2. The number of active sites was estimated using the catalyst concentration, which is equal to the number of moles of the catalyst used [49]; the amount of catalyst added was 10 mg. This was used to calculate the TON of the catalyst:

$$\text{TON} = \frac{\text{Amount of dye reacted (moles)}}{\text{Number of active sites (moles)}} \quad (1)$$

Table 2. The surface area, active sites and catalyst efficiency measures of the prepared nanoparticles.

Catalyst	Degradation Efficiency (%)	S _{BET} ^b (m ² /g)	Number of Active Sites (Moles)	TON ^a	TOF ^a (min ⁻¹)
nZVI (Fe ⁰)	72.13	47,092	3.60×10^{-5}	3.0631	0.2042
Fe/Cu 5:1	67.06	69,893	3.66×10^{-5}	2.7949	0.1863
Fe/Ag 5:0.1	22.79	51,952	3.64×10^{-5}	0.9561	0.0637
Fe/Cu/Ag 5:1:0.1	92.92	92,690	3.70×10^{-5}	3.8345	0.2556
Fe/Cu/Ag 5:1:0.2	100.00	104,420	3.74×10^{-5}	4.0879	0.2725
Fe/Cu/Ag 5:1:0.3	96.51	381,328	3.77×10^{-5}	3.9095	0.2606
Fe/Cu/Ag 5:1:0.4	98.36	397,073	3.80×10^{-5}	3.9498	0.2633
Fe/Cu/Ag 5:1:0.5	81.44	388,790	3.84×10^{-5}	3.2428	0.2162

^a TON and TOF were calculated using 10 mg catalyst loading and degradation efficiencies of the dye at 2 min reaction time. ^b BET surface area.

The TOF, which describes the number of moles of MO dye that a single catalyst active site can convert into products per unit time [50], was calculated using the following equation:

$$\text{TOF} = \frac{\text{TON}}{\text{time (min)}} \quad (2)$$

TON, and subsequently TOF, was determined using data at 2 min, which was the earliest point at which total MO degradation was attained (i.e., with the Fe/Cu/Ag 5:1:0.2 nanoparticles).

According to the results, the trimetallic nanoparticles had the highest amount of active sites as compared to the nZVI and the bimetallic nanoparticles. The number of active sites of the catalysts decreased in the following manner: Fe/Cu/Ag 5:1:0.5 > Fe/Cu/Ag 5:1:0.4 > Fe/Cu/Ag 5:1:0.3 > Fe/Cu/Ag 5:1:0.2 > Fe/Cu/Ag 5:1:0.1 > Fe/Cu 5:1 > Fe/Ag 5:0.1 > nZVI. The aforementioned observation corresponds well with the BET surface area

values obtained. It has been reported that catalysts with a high surface area possess high catalytic activity owing to an increase in accessible active sites [51,52]. The reported MO degradation efficiencies of the nanoparticles increased with an increase in BET surface area and number of active sites. However, the high surface area obtained with the trimetallic nanoparticles with Fe:Cu:Ag ratios above 5:1:0.2 did not lead to any enhancement in the MO degradation efficiency of the catalysts. This could imply that some of the reactive surface sites on the trimetallic nanoparticles were inaccessible or not directly involved in the catalytic reaction [53,54]. Moreover, adding Cu and Ag on the surface of nZVI led to an increase in surface area of the trimetallic nanoparticles.

The TOF and TON followed the same trend as the BET surface area, number of active sites and the degradation efficiency; in agreement with work previously reported by others [55], with all the trimetallic nanoparticles exhibiting the highest catalyst efficiency as measured by the TOF and TON. Furthermore, lower crystallite size has been directly linked to a high surface area and an improved catalytic activity [56], hence the observed trend which is in accordance with the crystallite sizes reported herein. Moreover, the Fe/Cu/Ag 5:1:0.2 nanoparticles have the highest TOF value (0.2752 min^{-1}) amongst the trimetallic systems, stipulating that their catalytic behavior was better than the other studied trimetallic systems, which was indeed the case as observed in Figure 5.

2.2.2. Parametric Tests on MO Dye Using Fe/Cu/Ag Nanoparticles

Effect of pH

Solution pH is known to be among the most significant variables influencing the degradation rate of MO dye with nZVI [1]. Thus, to study the influence of pH on the removal of MO, batch tests were performed at room temperature using Fe/Cu/Ag 5:1:0.2 nanoparticles at different pH values ranging from 3 to 9. The plot showing the effect of initial pH on MO dye degradation is illustrated in Figure 6. The observed degradation results at initial pH 3, 6, and 9 show that the degradation efficiency of methyl orange improved with a decrease in pH. These results show that the degradation of MO dye using the nZVI-based trimetallic nanoparticles is an acidic pH-driven process. This can be attributed to the fact that at higher pH, ferrous ions dissolved from the iron surface react with hydroxyl ions in an alkaline media, thereby producing ferrous hydroxide precipitation on the surface of iron invading the reactive sites and consequently inhibiting the reaction [57,58]. On the contrary, the increase in degradation rate of MO at low pH could be attributed to the ionization of the surface of nZVI and deprotonating of MO; the H^+ promotes the reduction of MO [59]. It can therefore be conclusively specified that acidic conditions are more favorable for the degradation process, as is expected with nZVI.

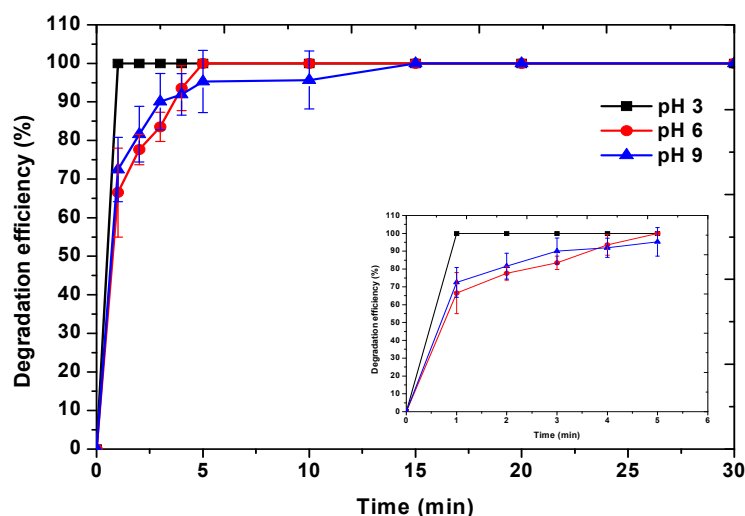


Figure 6. Degradation efficiencies of methyl orange dye (10 mg/L) using 10 mg Fe/Cu/Ag 5:1:0.2 nanoparticles with different pH conditions at room temperature.

Effect of Initial MO Dye Concentration

The initial concentrations of MO were evaluated for its degradation using Fe/Cu/Ag 5:1:0.2 at room temperature. As presented in Figure 7, the degradation of MO decreased as the initial MO concentration increased. The degradation reaches 100% in 30 min for the initial concentrations of 10, 25, and 50 mg/L, but it became slower as the initial concentration of MO increased further. At a low initial MO concentration (10 mg/L), the degradation efficiency was at 100% within 1 min into the reaction whilst at an elevated initial concentration (50 mg/L), the degradation only reached 100% after 30 min into the reaction. When the initial concentration was increased to 100 and 200 mg/L, the degradation efficiencies were even slower and did not reach 100% within 30 min. Moreover, for the initial MO concentration of 200 mg/L, the degradation efficiency reached saturation (86%) at 20 min reaction time. The decline in degradation as MO concentration increases can be ascribed to adsorption competition among dye molecules on the inadequate reaction sites of the nanoparticles at a greater concentration of MO dye [1]. Furthermore, an increase in reaction intermediates could be produced by the higher concentration of MO reducing the active sites available for the degradation of MO [30]. These results are in line with what other authors have reported on the effect of initial pollutant concentration in its degradation using nZVI-based nanoparticles. For example, Chen et al. [59] reported that an increase in dye concentration effectuates a decrease in the removal efficiency of MO using bentonite-supported nZVI. Moreover, studies involving bimetallic nZVI-based nanoparticle such as Fe/Ag on the degradation of tetrabromobisphenol [34] and Fe/Cu on orange II degradation [37] also showed similar results to what was reported above. The degradation efficiency of the pollutants, as reported in these afore-mentioned studies, was found to be restricted by increased initial concentration of the pollutants.

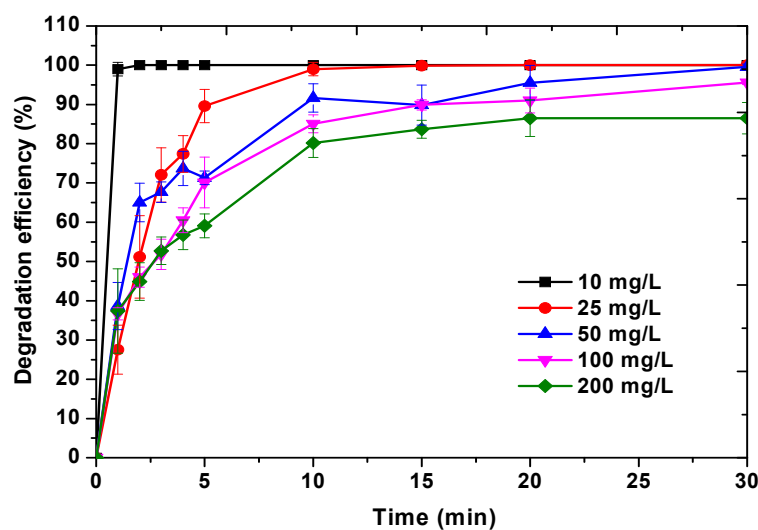


Figure 7. Degradation efficiencies of methyl orange dye using 10 mg Fe/Cu/Ag 5:1:0.2 nanoparticles with different initial MO concentrations (pH ~ 4.5) at room temperature.

Effect of Initial Fe/Cu/Ag Nanoparticle Dosage

The effect of nanoparticle dosage on MO was investigated with three different dosages (4, 7, and 10 mg) at MO concentration of 10 mg/L. As depicted in Figure 8, the degradation efficiency of MO increases with an increase in nanoparticle dosage. Higher degradation efficiency was obtained using higher Fe/Cu/Ag 5:1:0.2 nanoparticle dosage, which was 10 mg. When 4 mg of Fe/Cu/Ag 5:1:0.2 nanoparticles was used, only 85% of the dye was degraded in the first 10 min while the other two loadings reached 100% within 10 min. It can be interpreted that the dosage of Fe/Cu/Ag 5:1:0.2 nanoparticles increased the number of active sites leading to enhanced degradation of the MO dye [33].

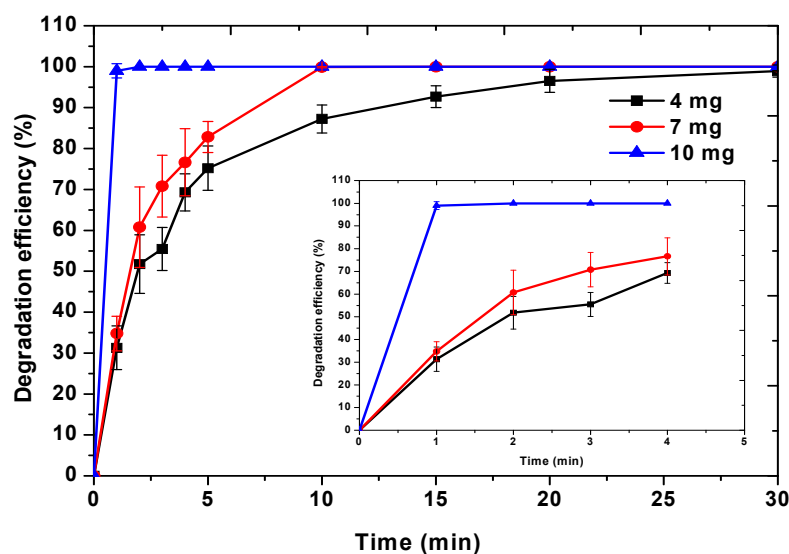


Figure 8. Degradation efficiencies of 10 mg/L methyl orange dye (pH ~ 4.5) by Fe/Cu/Ag 5:1:0.2 nanoparticles with varying nanoparticle dosage at room temperature.

2.3. Catalyst Reusability Studies

The stability and reusable capability of Fe/Cu/Ag 5:1:0.2 nanoparticles were investigated in three consecutive cycles under the same experimental conditions. As presented in Figure 9, the degradation efficiency of MO using the nanoparticles decreases after every run. The results show that the effectiveness of the nanoparticles reduces in consecutive experiments from 100% to 54% in run 3 within 30 min. The observed results are the norm in catalytic reactions; for example, a study by Wang et al. [30] observed a similar trend, except that the depreciation in the efficiency of Fe/Cu nanoparticles was relatively slower as compared to that reported in this study. Similarly, Shen et al. [60] used bimetallic Fe/Cu nanoparticles for the removal of nitrate in water. The reusability of the Fe/Cu nanoparticles was found to be relatively poor compared to when the catalyst was regenerated using HCl and NaBH₄ to restore the zerovalent state of the catalyst metals. However, without the regeneration, the removal of nitrate declined from about 95% in the first cycle to about 5% in the third cycle. Thus, the reducing efficacy during degradation can be ascribed to the alteration in the oxidation state of the active catalyst induced by the presence of oxygen in water and catalyst contamination by methyl orange degradation byproducts [30,39,61]. As a result, the regeneration of the nanoparticles using the reducing agent minimizes the depreciation in the activity of the nanoparticles upon reuse, when compared to merely washing the nanoparticles in ethanol and then reusing them [62,63]. Moreover, according to Navalon et al. [64], catalyst reusability depends on the amount of the solid used and using smaller amounts of catalyst would make the reusability challenging. Thus, that could be the reason why the catalyst in this study only showed a great reusability capacity in run 2 which then decreased by about 40% in the third run. Furthermore, the drastic decrease in the degradation efficiency in the third run is ascribed to the exposure of nanoparticles to air during washing after degradation tests. Nevertheless, the great degradation efficiency in run 2 demonstrated that the fabricated Fe/Cu/Ag 5:1:0.2 shows potential reusability capability. The nanoparticles might not be stable enough to be reused multiple times without regeneration with a reducing agent.

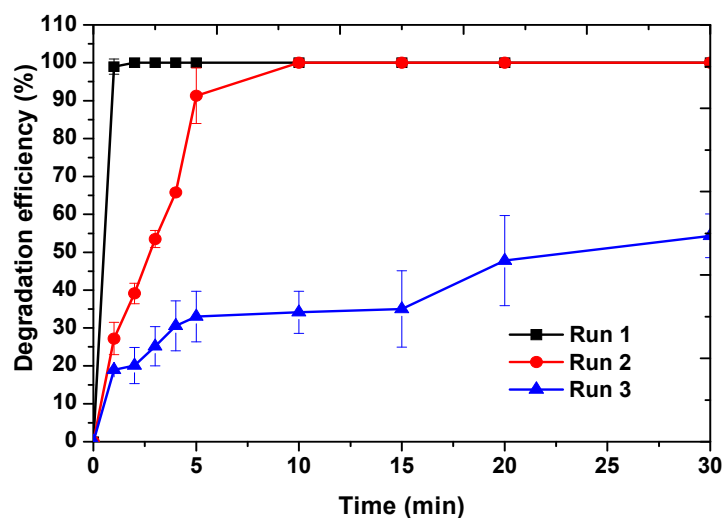


Figure 9. Degradation efficiencies of 10 mg/L methyl orange (pH= ~ 4.5) using 10 mg Fe/Cu/Ag 5:1:0.2 nanoparticles for 30 min in different batch runs.

2.4. Reaction Kinetics of the Degradation of Methyl Orange

The degradation results were fitted on the following kinetic models; zeroth, first, pseudo-first, and second order. Based on the data acquired, the kinetics of MO degradation has more correlation with the pseudo-first order model. In which case, it is the kinetic measurement of a second order reaction, using an excess of one reactant in order to produce more precise results as only one analyte concentration (MO) could be accurately quantified [65]. Thus, the kinetics were investigated using the pseudo first-order kinetics model which is mostly used to evaluate the degradation of azo dyes using nZVI nanoparticles in other studies [58,66], the rate (v) can be expressed as:

$$v = -\frac{dC}{dt} = k_{SA}a_s\rho_m C \quad (3)$$

where k_{SA} , a_s , ρ_m are constant for a specific reaction and can therefore be expressed as a single parameter k_{obs} , which is the pseudo first-order observed rate constant. Equation (3) can be integrated into the equation given below:

$$\ln \frac{C}{C_0} = -k_{obs}t \quad (4)$$

where C is the MO dye concentration at a certain time t , C_0 is the initial MO dye concentration and k_{obs} is the pseudo first-order reaction observed rate constant which can be determined from the slope of the plot $\ln C/C_0$ versus time (min). The regression lines were achieved from the aforementioned plot with a correlation coefficient (R^2) of over 0.865 for all three parameters as shown in Table 3; which confirms that the degradation of MO by Fe/Cu/Ag 5:1:0.2 fitted the pseudo first-order kinetic model. The rate constant (k_{obs}) decreases with an increase in pH in the following order: pH 3 (0.7177 min^{-1}) > pH 6 (0.3930 min^{-1}) > pH 9 (0.2353 min^{-1}) (Figure 10a and Table 3). It is therefore clear that the initial solution pH is a significant parameter that affects the kinetics in the degradation of methyl orange dye by Fe/Cu/Ag 5:1:0.2 nanoparticles. Furthermore, Figure 10b shows the effect of nanoparticle dosage on the kinetics of MO dye degradation by Fe/Cu/Ag 5:1:0.2 nanoparticles. The rate constant increases linearly with an increase in nanoparticle dosage in the following order: 4 mg (0.1371 min^{-1}) < 7 mg (0.2408 min^{-1}) < 10 mg (0.6663 min^{-1}) due to an increased reactive surface area [67]. Lastly, the effect of initial MO concentration on degradation is shown in Figure 10c. The rate constant obtained decreases with an increase in dye concentration: 10 mg/L (0.6663 min^{-1}) > 25 mg/L (0.4576 min^{-1}) > 50 mg/L

(0.1798 min^{-1}) > 100 mg/L (0.1714 min^{-1}) > 200 mg/L (0.1420 min^{-1}). Similar results as above were also reported in previous studies [57,66,67].

Table 3. Summary of R^2 and pseudo first-order rate constant of the studied parameters in MO degradation using Fe/Cu/Ag 5:1:0.2.

Parameters		R^2	$k_{obs} (\text{min}^{-1})$
pH	3 ^a	0.897	0.7177
	6	0.996	0.3930
	9	0.873	0.2353
Nanoparticle dosage (mg)	4	0.934	0.1371
	7	0.987	0.2408
	10 ^a	0.865	0.6663
Initial dye concentrations (mg/L)	10 ^a	0.865	0.6663
	25	0.995	0.4576
	50	0.901	0.1798
	100	0.964	0.1714
	200	0.941	0.1420

^a The rate constants were calculated after 2 min due to the rapid degradation as opposed to the other conditions.

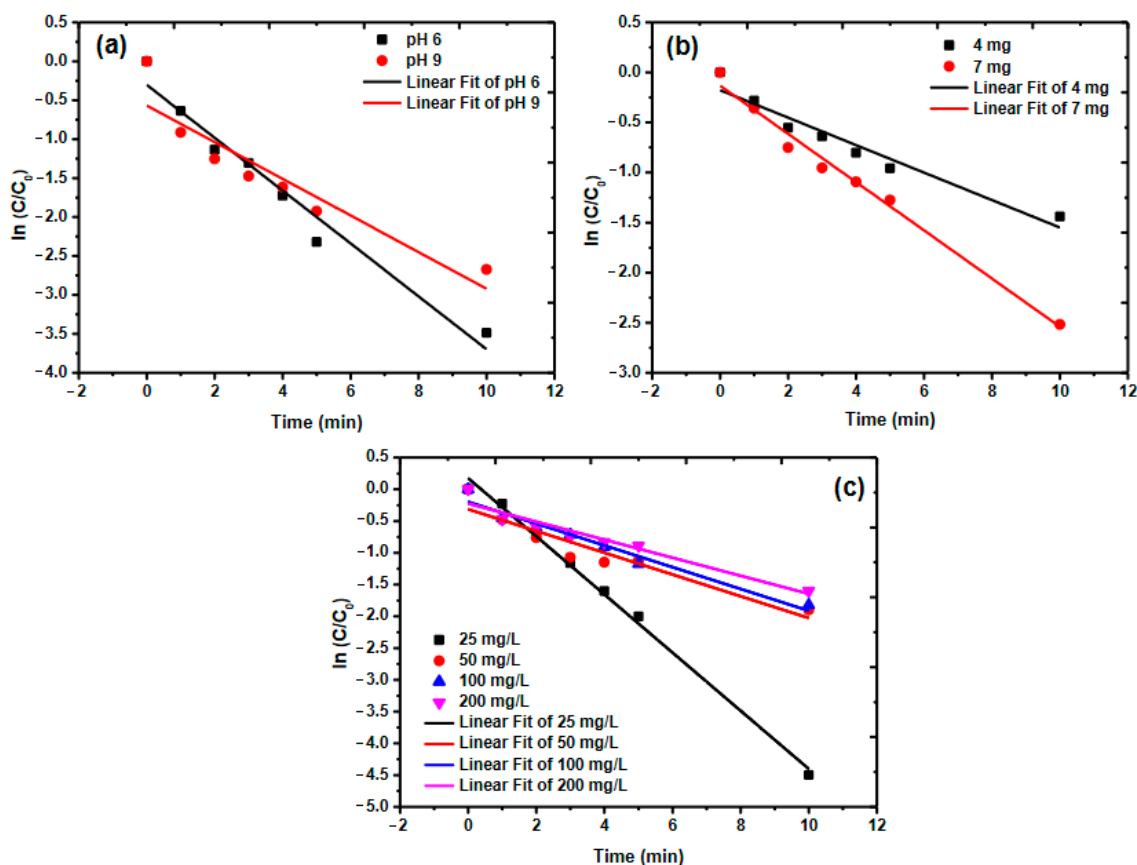


Figure 10. Pseudo first-order kinetics of MO degradation using Fe/Cu/Ag 5:1:0.2 nanoparticles varying the (a) pH, (b) nanoparticle dosage and (c) Initial MO concentration.

2.5. Degradation Products and Pathway

The degradation products of methyl orange dye by the Fe/Cu/Ag nanoparticles were identified using LC-MS analysis. Figure 11 shows the total mass spectrograms of MO at 0, 5, and 30 min of degradation by Fe/Cu/Ag 5:1:0.2 nanoparticles. It can be observed that at 0 min (Figure 11a), there is a characteristic peak at m/z 306 that is assigned

to the positive ion of the MO dye. However, the chromatogram of the degraded MO at 1 min showed a complete disappearance of the MO peak at 2.02 min retention time (Figure A3). This observation is a confirmation of the UV-vis (Figure A2) results that presented 100% degradation efficiency within 1 min of contact with the nanoparticles. Thus, the mass spectrogram at 5 min (Figure 11b) of degradation shows new m/z peaks at 121, 136, 157, and 172 that correspond to the intermediate products from MO degradation. The products that were formed are sulfanilic acid at m/z 172 which further fragmented into benzenesulfonic acid at m/z 157 after losing an amino group (NH_2) and N,N -dimethyl- p -phenylenediamine at m/z 136 which further fragmented into N,N -dimethylbenzenamine at m/z 121 after losing an amino group (NH_2). Figure 11c shows the degradation at 30 min and only one product at m/z 157 (benzenesulfonic acid) is observed and decreased by about 50% of the intensity observed at 5 min. The peak at m/z 282 was unidentified as it does not correspond to any of the masses of the MO, any other known MO degradation byproducts, the catalyst used in the experiment, or the combination of the catalyst and the products. Thus, it can be stipulated that it is an anomalous peak emanating from impurities from the column, metal ions such as Cu or Fe from the sample itself (in this case) or the autosampler [68,69]. Moreover, the observed results are in line with what other researchers have reported for the degradation of MO using Fe-based particles [58,70]. However, in this study, MO was completely degraded within 1 min into the reaction, which was faster than previously reported MO degradation results using Fe-based bimetallic nanoparticles [71]. From the observed results, it can be concluded that MO degradation pathway possibly involved the symmetric cleavage of the azo bond ($-\text{N}=\text{N}-$); producing sulfanilic acid and N,N -dimethyl- p -phenylenediamine, which was followed by further degradation of the intermediate products. As shown in Figure 12, unlike MO, the products from MO degradation might be further mineralized into CO_2 and H_2O in the presence of other parameters such as $\bullet\text{OH}$ radicals and high temperature [19,72].

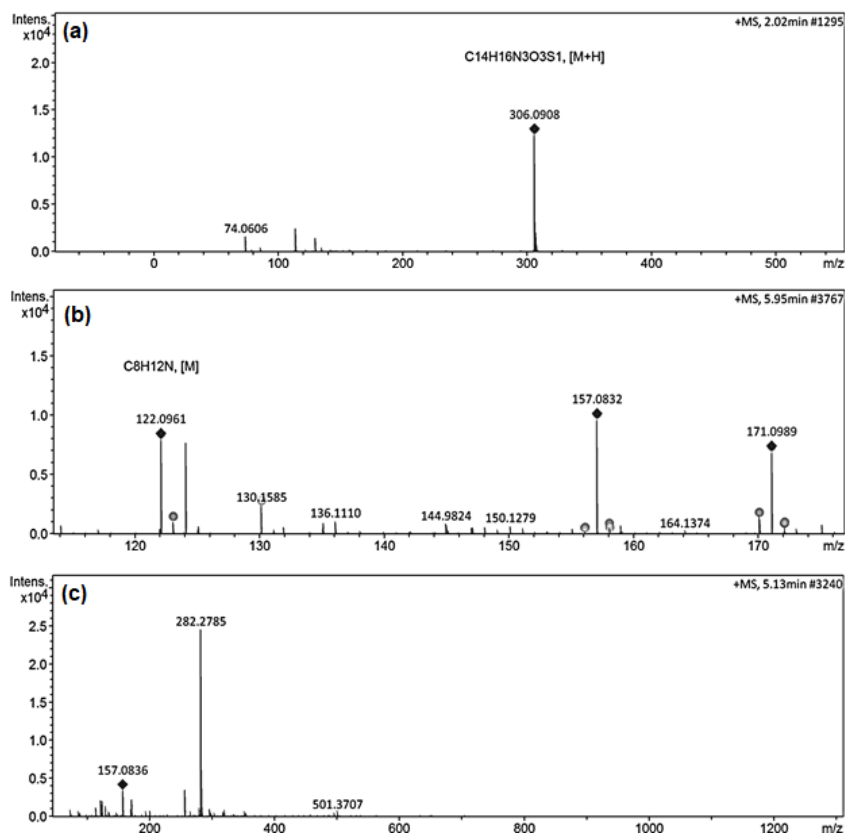


Figure 11. LC-MS analysis of MO dye degradation using Fe/Cu/Ag 5:1:0.2 at (a) 0 min (b) 5 min and (c) 30 min.

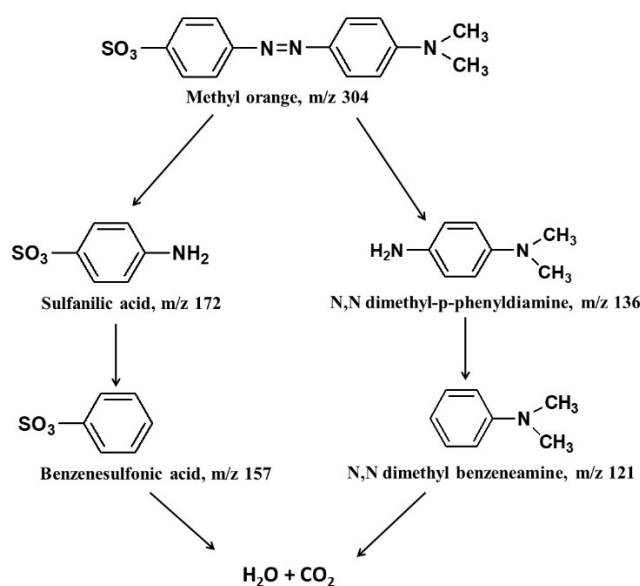


Figure 12. Possible reaction pathway of MO degradation.

3. Materials and Methods

3.1. Materials

The precursor for iron nanoparticles: iron sulphate heptahydrate ($\text{FeSO}_4 \cdot 7\text{H}_2\text{O}$, $\geq 99.0\%$), the reducing agent: sodium borohydride (NaBH_4 , $\geq 98.0\%$), the surfactant polyvinylpyrrolidone (PVP, MW 40,000), hydrochloric acid (HCl, 37.0%), and sodium hydroxide pellets ($\text{NaOH} \geq 98.0\%$) were all obtained from Sigma Aldrich, Johannesburg, South Africa. The silver nanoparticles precursor: silver nitrate ($\text{AgNO}_3 > 99.5\%$ purity) was obtained from the Radchem, Johannesburg, South Africa. The copper nanoparticles precursor: cupric sulphate pentahydrate ($\text{CuSO}_4 \cdot 5\text{H}_2\text{O}$) and methyl orange dye were both from ACE Chemicals, Johannesburg, South Africa. Absolute ethanol (99.9%) was obtained from Kayla Africa Suppliers and Distributors, Johannesburg, South Africa. All the chemicals and materials were used without additional purification. Deionized water was used throughout the entire experimental process.

3.2. Synthesis of the Nanoparticles

The nanoparticles were synthesized using the sodium borohydride chemical reduction method. In the preparation of Fe/Cu/Ag nanoparticles, 1 g of PVP was first weighed in a three-neck round-bottom flask (500 mL) containing a stirrer bar with 50 mL ethanol and 50 mL of water. The mixture was placed on a stirrer plate and supplied with a fixed stream of nitrogen gas to eliminate oxygen that could interfere with the reaction by forming oxides. After 30 min, 5.57 g of $\text{FeSO}_4 \cdot 7\text{H}_2\text{O}$ was added into the mixture and stirred for a further 30 min. Then 0.945 g of NaBH_4 was added into a 25 mL volumetric flask and filled up with high purity water and drop-wisely added into the $\text{FeSO}_4 \cdot 7\text{H}_2\text{O}$ mixture to produce black nanoscale zerovalent iron (Fe^0) nanoparticles. Thereafter, 1 g of $\text{CuSO}_4 \cdot 5\text{H}_2\text{O}$ and 0.068 g of AgNO_3 were both added into a 100 mL volumetric flask and filled to the mark with high purity water. The solution was added into the iron nanoparticles after 30 min and continually stirred. After a further 30 min, NaBH_4 solution prepared as above was added into the mixture to produce Fe/Cu/Ag 5:1:0.2 nanoparticles. After stirring for a further 30 min, the nanoparticles were removed from the stirrer and subsequently placed into centrifuge tubes. The nanoparticles were washed 3 times in ethanol to remove excess nanoparticle precursors and NaBH_4 , and residual PVP. After washing, the nanoparticles were dried at 25 °C overnight under a vacuum. For optimization purposes, the amount of silver was varied and the following Fe/Cu/Ag molar ratios were prepared: 5:1:0.1, 5:1:0.2, 5:1:0.3, 5:1:0.4, and 5:1:0.5. Bimetallic Fe/Cu (5:1) and Fe/Ag (5:0.1) as well as nZVI

nanoparticles were also synthesized as above. Figure 13 shows a summary of the addition of the precursors for each of the nanoparticles synthesized.

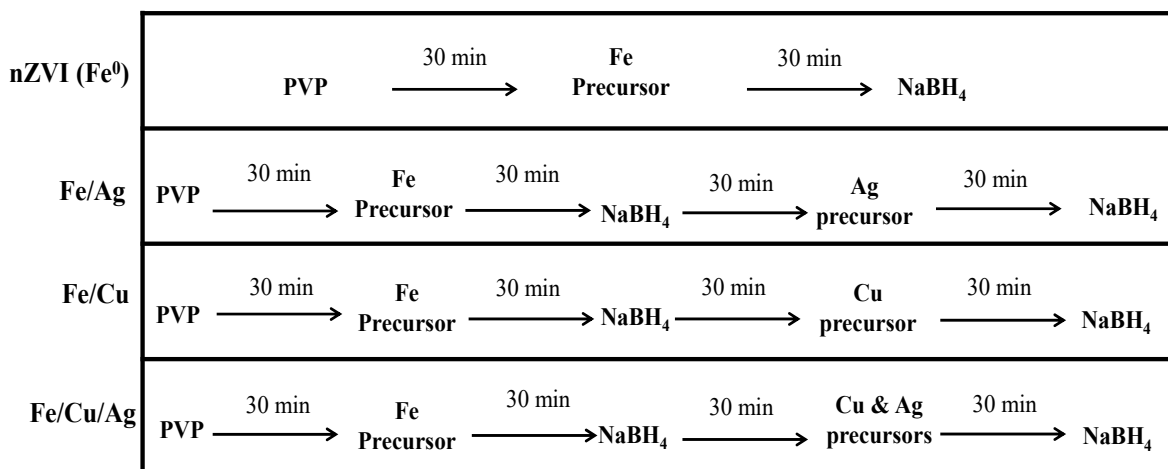


Figure 13. Summary of precursor addition sequence of the nanoparticle synthesis procedure.

3.3. Degradation Studies and Sample Analysis

A series of batch degradation experiments of methyl orange dye (MO) were conducted to determine the catalytic activity of the nanoparticles. All degradation tests were carried out at room temperature in an open-batch system. About 50 mL of MO dye solution (10 mg/L) was poured into a 100 mL beaker equipped with a stirrer bar and stirred on a stirrer plate at 250 rpm for 30 min. Thereafter, 10 mg of the prepared nanoparticles was added onto the MO dye and stirred at 250 rpm. Samples were drawn into small centrifuge tubes at the following time intervals: 1, 2, 3, 4, 5, 10, 15, 20, and 30 min. These samples were then centrifuged for about 15 min to isolate the prepared nanoparticles from the supernatant. The used particles were collected using a centrifuge then washed in ethanol 3 times and dried in a vacuum oven for reusability studies. For the parametric tests, the pH, nanoparticle dosage, and initial MO dye concentration were varied. The pH of the solution was modified from 3 to 9 using HCl and NaOH. The nanoparticle dosages studied were 4, 7, and 10 mg. While the initial dye concentrations studied were 10, 25, 50, 100, and 200 mg/L. The parametric tests were performed under the same experimental conditions as above. The degradation efficiency was determined using the following:

$$\text{Degradation (\%)} = \frac{A_0 - A_t}{A_0} \times 100 \quad (5)$$

where A_0 is the MO dye absorbance before degradation and A_t is the MO dye absorbance after certain time t .

3.4. Characterization

Powder X-ray Diffraction (p-XRD) measurements of the nanoparticles were conducted using Bruker AXS D8 (Bruker, Johannesburg, South Africa) X-ray advanced powder diffractometer operating at 40 kV and 35 mA ($\lambda = 1.78897 \text{ \AA}$). The diffraction patterns were recorded with a scanning speed of $0.02^\circ/\text{s}$ in the 2θ range of 10 to 75° diffraction angle. The powder diffractometer was fitted with a nickel filter and a LinxEye detector (Bruker, Johannesburg, South Africa). The crystallite sizes (D) of the synthesized nanoparticles were calculated using the Scherrer equation given below:

$$D = \frac{K\lambda}{\beta \cos\theta} \quad (6)$$

where K is the proportionality constant, λ is the wavelength of the diffractometer, θ is the Bragg's angle (in radians), and β is the peak's full width at half maximum (FWHM) [36,73].

An X-ray photoelectron spectroscopy (XPS) analysis of the nanoparticles was performed using a Thermo Fisher Scientific ESCALab 250Xi (Thermo Fisher Scientific, Johannesburg, South Africa) with monochromatic Al $K\alpha$ at 1486.7 eV running at 300 W of power to identify different elements in the nanoparticles. The hemispherical electron energy analyzer with a spot size of 100 μm worked in the constant analyzer energy (CAE) mode at an analyzer pass energy of 100 eV for the wide range XPS spectra and 20 eV for the high-resolution narrow scan of each element.

Transmission Electron Microscopy (TEM) analyses coupled with Energy Dispersion X-ray spectroscopy (EDX) were conducted on a JEOL JEM-2100F (JEOL, Tokyo, Japan) field emission electron microscope. The samples were suspended in ethanol by ultrasonication and then dropped on a 300 mesh formvar-coated nickel grid. The particle sizes of the nanoparticles observed on TEM were estimated using ImageJ.

The dye solutions were analyzed using a Thermo Fisher Scientific, Multiskan GO, UV-vis Microplate Spectrophotometer (Thermo Fisher Scientific, Vantaa, Finland). Methyl orange concentrations in the solutions were quantified by the use of the absorption peak at wavelength of 464 nm.

The surface areas of the nanoparticles were determined using the Brunauer-Emmett-Teller (BET) method from Nitrogen physisorption analysis conducted at $-196\text{ }^\circ\text{C}$ (77 K) using a Micromeritics TriStar 3000 V6.05 A (Micromeritics Instrument Corporation, Norcross, GA, USA).

The identification of methyl orange degradation products was performed on a Bruker Compact Q-TOF high resolution Liquid Chromatography-Mass Spectroscopy (LC-MS) (Bruker, Johannesburg, South Africa). Separations were obtained under isocratic conditions using a Luna Omega 1.6 μm C18 column (50 \times 2.1 mm) (Separations Scientific SA (Pty) Ltd., Johannesburg, South Africa) and a mobile phase composed of 0.1% formic acid, in both acetonitrile and water; flow rate 0.3 mL/min. A 20 μL volume of sample was injected using the autosample system. The MS was coupled with an electrospray ionization source (ESI) and ran at positive polarity. The ESI conditions were in the following manner: capillary voltage = 4500 V, endplate offset = -500 V, nebulizer pressure = 1.8 bar, drying gas flow = 9.0 L/min, temperature = $220\text{ }^\circ\text{C}$ and mass range = 50–1300 m/z .

4. Conclusions

In this work, Fe/Cu/Ag 5:1:0.2 trimetallic nanoparticles were successfully synthesized using the sodium borohydride reduction method and characterized by surface sensitive and surface specific techniques. The TEM images showed a chain-like structure with core-shells that consist of iron in the core and a mixture of Cu, Ag, and Fe oxides in the shell. Experiments displayed that the degradation efficiency of the Fe/Cu/Ag trimetallic nanoparticles (100% in 1 min) was higher than that of the bimetallic Fe/Cu (100% in 10 min) and Fe/Ag (68% in 15 min) nanoparticles, proving that trimetallic nanoparticles provide faster degradation efficiencies of the MO dye compared to their bimetallic counterparts. The catalytic efficiency of the nanoparticles was proposed using the number of active sites and TOF in dye degradation; the optimal trimetallic system Fe/Cu/Ag 5:1:0.2 had a TOF value of 0.2752 min^{-1} . Moreover, batch experiments illustrate that initial MO dye concentration, nanoparticle dosage, and solution pH did affect the degradation efficiency of MO using the Fe/Cu/Ag nanoparticles. A lower pH value, high nanoparticle dosage, and lower initial MO concentration were more favorable for the catalytic degradation of MO dye. The degradation followed a pseudo first-order kinetic model. Furthermore, the pseudo first-order rate constant increased with a decrease in pH and initial MO dye concentration and increased with an increase in nanoparticle dosage. The results of LC-MS show that the degradation of methyl orange occurs within 1 min, yielding aromatic products that are more prone to mineralization. Lastly, the Fe/Cu/Ag trimetallic nanoparticles could be potentially reusable when used in larger quantities and have in this study been demonstrated to

possess the capability to be used for remediation of textile dye wastewater. The application of these nanoparticles in industrial scale applications will require the nanoparticles to be immobilized in a membrane substrate to reduce the possibility of agglomeration, owing to the high magnetic properties, and enhance reusability and recoverability.

Author Contributions: Conceptualization, K.S., G.N. and N.M.; Data curation, K.S.; Formal analysis, M.K. and G.N.; Funding acquisition, K.S.; Investigation, M.K.; Methodology, M.K., K.S. and G.N.; Project administration, N.M.; Resources, K.S. and N.M.; Supervision, K.S., G.N. and N.M.; Validation, K.S., G.N. and N.M.; Visualization, K.S. and N.M.; Writing—original draft, M.K.; Writing—review & editing, K.S., G.N. and N.M. All authors have read and agreed to the published version of the manuscript.

Funding: The financial support of Mintek and the Department of Science and Innovation/Mintek Nanotechnology Innovation Centre is gratefully acknowledged.

Acknowledgments: The authors would also like to thank the University of the Witwatersrand and the Department of Science and Innovation/Mintek Nanotechnology Innovation Centre for their support and research facilities.

Conflicts of Interest: The authors declare no conflict of interest.

Appendix A

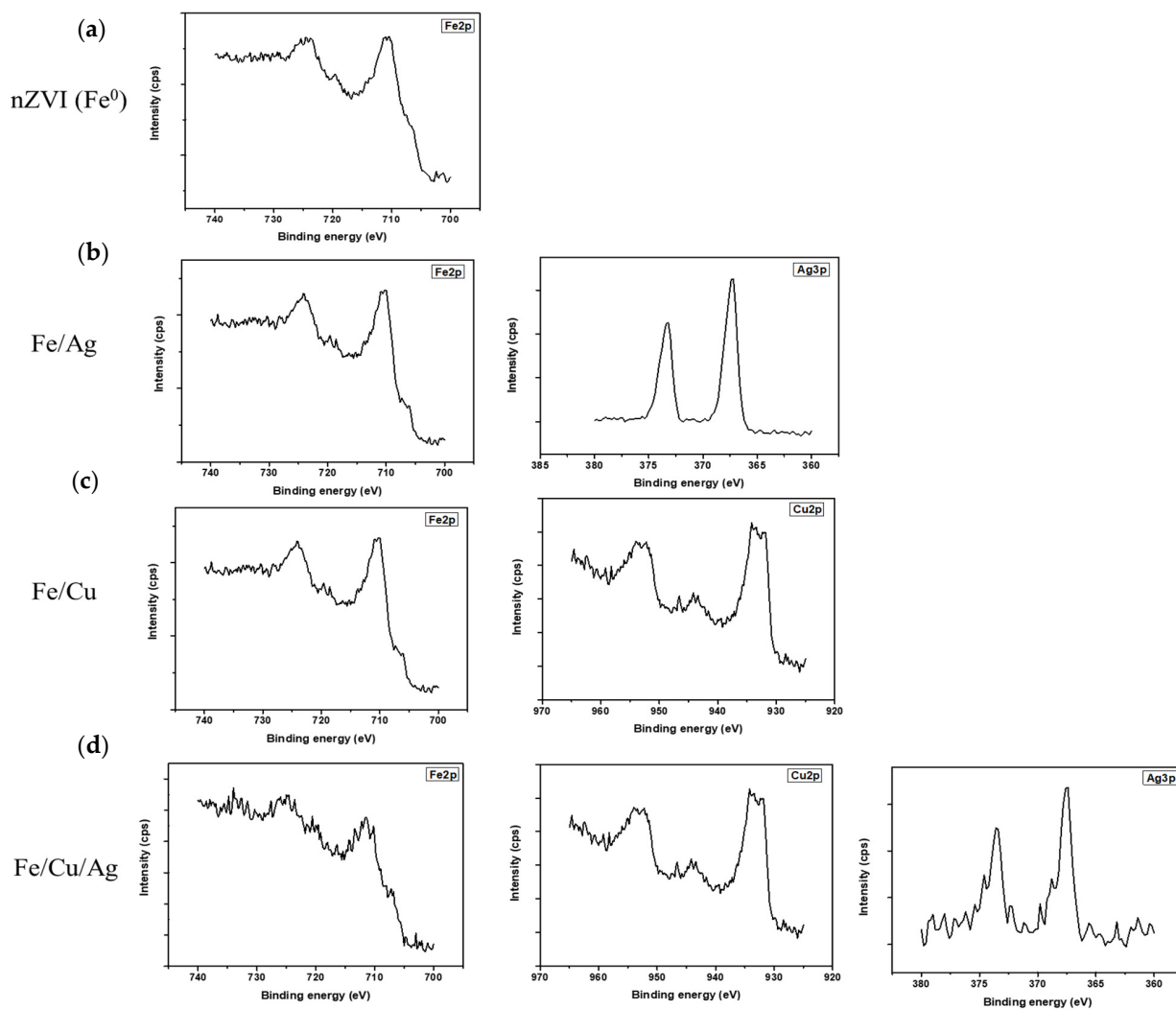


Figure A1. XPS narrow scan spectra of the nanoparticles: (a) Fe⁰/nZVI-Fe₂p, (b) Fe/Ag (5:0.1)-Fe₂p and Ag₃d, (c) Fe/Cu (5:1)-Fe₂p and Cu₂p and (d) Fe/Cu/Ag (5:1:0.2)-Fe₂p, Cu₂p and Ag₃d.

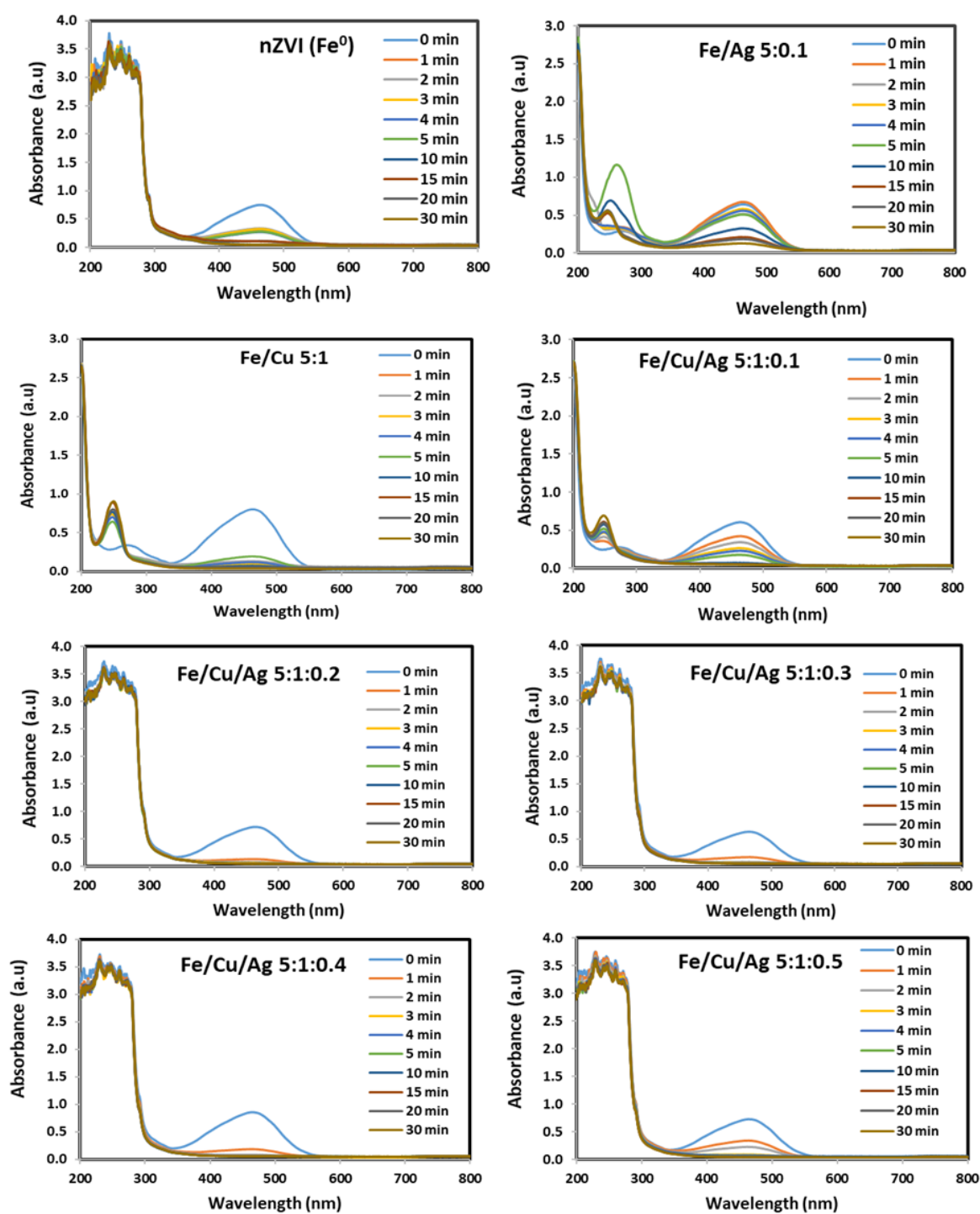
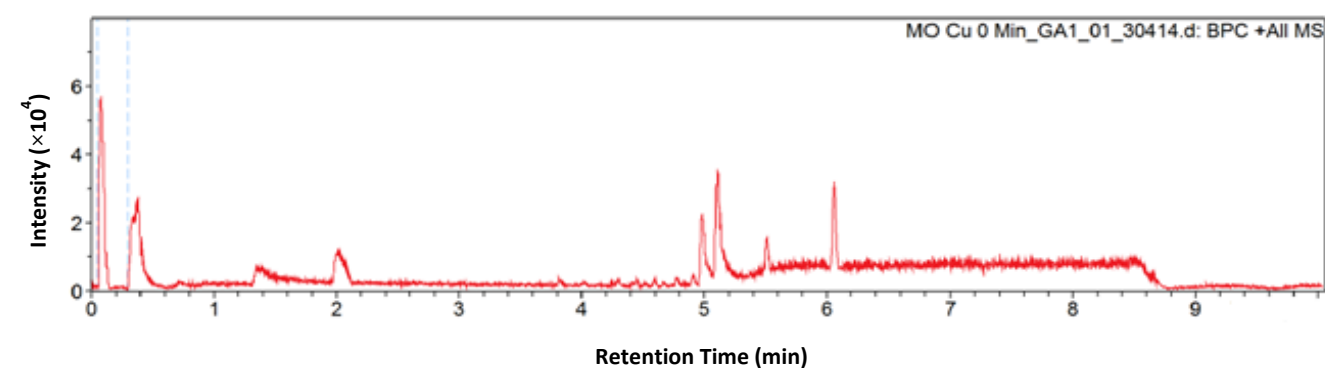
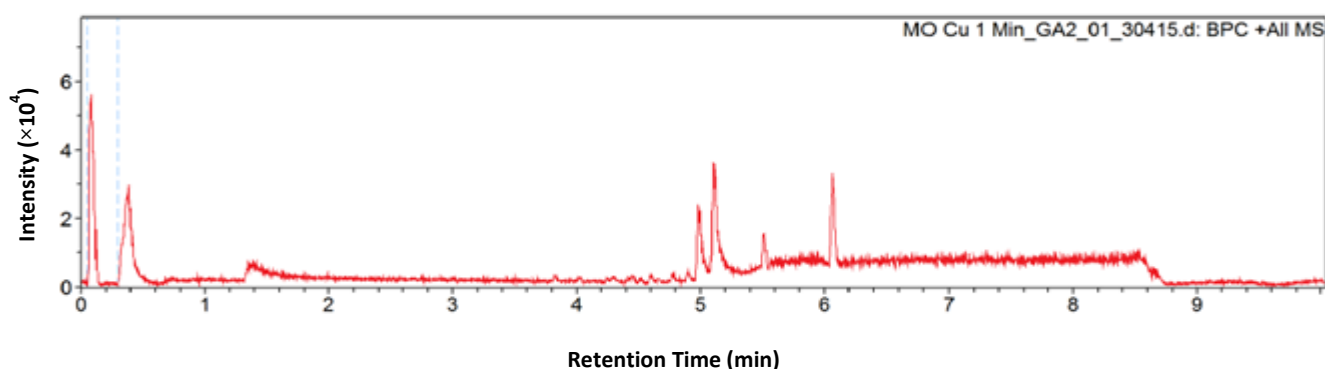


Figure A2. UV-vis absorption spectra of MO dye degradation by nZVI, bimetallic Fe/Ag (5:0.1), bimetallic Fe/Cu (5:1) and trimetallic Fe/Cu/Ag (5:1:0.1), (5:1:0.2), (5:1:0.3), (5:1:0.4) and (5:1:0.5) nanoparticles for 30 min.



(a)



(b)

Figure A3. Mass chromatogram of methyl orange solution (a) before degradation at 0 min and (b) after 1 min degradation by Fe/Cu/Ag 5:1:0.2 nanoparticles.

References

1. El-Sayed, E.M.; Elkady, M.F.; El-Latif, M.M.A. Biosynthesis and characterization of zerovalent iron nanoparticles and its application in azo dye degradation. *Indian J. Chem. Technol.* **2017**, *24*, 541–547.
2. Ahuja, N.; Chopra, A.K.; Ansari, A.A. Removal of Colour from aqueous solutions by using zero valent iron nanoparticles. *IOSR J. Environ. Sci. Toxicol. Food Technol.* **2016**, *10*, 4–14.
3. Nandhini, N.T.; Rajeshkumar, S.; Mythili, S. The possible mechanism of eco-friendly synthesized nanoparticles on hazardous dyes degradation. *Biocatal. Agric. Biotechnol.* **2019**, *19*, 101–138. [[CrossRef](#)]
4. Gupta, V.K.; Jain, R.; Nayak, A.; Agarwal, S.; Shrivastava, M. Removal of the hazardous dye- Tartrazine by photodegradation on titanium dioxide surface. *Mater. Sci. Eng. C* **2011**, *31*, 1062–1067. [[CrossRef](#)]
5. Liu, H.L.; Chiou, Y.R. Optimal decolorization efficiency of Reactive Red 239 by UV/TiO₂ photocatalytic process coupled with response surface methodology. *Chem. Eng. J.* **2005**, *112*, 173–179. [[CrossRef](#)]
6. Asouhidou, D.D.; Triantafyllidis, K.S.; Lazaridis, N.K.; Matis, K.A.; Kim, S.S.; Pinnavaia, T.J. Sorption of reactive dyes from aqueous solutions by ordered hexagonal and disordered mesoporous carbons. *Microp. Mesop. Mater.* **2009**, *117*, 257–267. [[CrossRef](#)]
7. Alver, E.; Metin, A.Ü. Anionic dye removal from aqueous solutions using modified zeolite: Adsorption kinetics and isotherm studies. *Chem. Eng. J.* **2012**, *200–202*, 59–67. [[CrossRef](#)]
8. Xingu-Contreras, E.; García-Rosales, G.; Cabral-Prieto, A.; García-Sosa, I. Degradation of methyl orange using iron boride nanoparticles supported in a natural zeolite. *Environ. Nanotechnol. Monit. Manag.* **2017**, *7*, 121–129. [[CrossRef](#)]
9. Rahman, N.; Abedin, Z.; Hossain, M.A. Rapid degradation of azo dyes using nano-scale zero valent iron. *J. Environ. Sci.* **2014**, *10*, 157–163. [[CrossRef](#)]
10. Freyria, F.S.; Esposito, S.; Armandi, M.; Deorsola, F.; Garrone, E.; Bonelli, B. Role of pH in the Aqueous Phase Reactivity of Zerovalent Iron Nanoparticles with Acid Orange 7, a Model Molecule of Azo Dyes. *J. Nanomater.* **2017**, *2017*, 1–13. [[CrossRef](#)]
11. Raman, C.D.; Kanmani, S. Textile dye degradation using nano zero valent iron: A review. *J. Environ. Manag.* **2016**, *177*, 341–355. [[CrossRef](#)]
12. Chatterjee, S.; Lim, S.R.; Woo, S.H. Removal of Reactive Black 5 by zero-valent iron modified with various surfactants. *Chem. Eng. J.* **2010**, *160*, 27–32S. [[CrossRef](#)]

13. Lai, B.; Zhou, Y.X.; Yang, P. Passivation of sponge iron and GAC in Fe⁰/GAC mixed-potential corrosion reactor. *Ind. Eng. Chem. Res.* **2012**, *51*, 7777–7785. [[CrossRef](#)]
14. Yuan, Y.; Yuan, D.; Zhang, Y.; Lai, B. Exploring the mechanism and kinetics of Fe-Cu-Ag trimetallic particles for p-nitrophenol reduction. *Chemosphere* **2017**, *186*, 132–139. [[CrossRef](#)] [[PubMed](#)]
15. Kaur, P.; Thakur, R.; Malwal, H.; Manuja, A.; Chaudhury, A. Biosynthesis of biocompatible and recyclable silver/iron and gold/iron core-shell nanoparticles for water purification technology. *Biocatal. Agric. Biotechnol.* **2018**, *14*, 189–197. [[CrossRef](#)]
16. Bokare, A.D.; Chikare, R.C.; Rode, C.V.; Paknikar, K.M. Effect of surface chemistry of Fe-Ni nanoparticles on mechanistic pathways of azo dye degradation. *Environ. Sci. Technol.* **2007**, *41*, 7437–7443. [[CrossRef](#)]
17. Smuleac, V.; Varma, R.; Sikdar, S.; Bhattacharyya, D. Green Synthesis of Fe and Fe/Pd bimetallic nanoparticles in membranes for reductive degradation of chlorinated organics. *J. Memb. Sci.* **2011**, *379*, 131–137. [[CrossRef](#)]
18. Kirichenko, O.; Kapustin, G.; Nissenbaum, V.; Mishin, I.; Kustov, L. Evaluation of stability of silica-supported Fe-Pd and Fe-Pt nanoparticles in aerobic conditions using thermal analysis. *J. Therm. Anal. Calorim.* **2014**, *118*, 749–758. [[CrossRef](#)]
19. Wang, Y.; Zhao, H.; Zhao, G. Iron-copper bimetallic nanoparticles embedded within ordered mesoporous carbon as effective and stable heterogeneous Fenton catalyst for the degradation of organic contaminants. *Appl. Catal. B Environ.* **2015**, *164*, 396–406. [[CrossRef](#)]
20. Ruíz-Baltazar, A.; Esparza, A.R.; Pérez, R.; Rosas, G. Structural characterization of Fe-Ag bimetallic nanoparticles synthesized by chemical reduction. *Int. Res. J. Pure Appl. Chem.* **2014**, *4*, 263–269. [[CrossRef](#)]
21. Mossa Hosseini, S.; Ataie-Ashtiani, B.; Kholghi, M. Nitrate reduction by nano-Fe/Cu particles in packed column. *Desalination* **2011**, *276*, 214–221. [[CrossRef](#)]
22. Li, T.; Farrell, J. Reductive Dechlorination of trichloroethene and carbon tetrachloride using iron and palladized-iron cathodes. *Environ. Sci. Technol.* **2000**, *34*, 173–179. [[CrossRef](#)]
23. Bransfield, S.J.; Cwiertny, D.M.; Livi, K.; Fairbrother, D.H. Influence of transition metal additives and temperature on the rate of organohalide reduction by granular iron: Implications for reaction mechanisms. *Appl. Catal. B Environ.* **2007**, *76*, 348–356. [[CrossRef](#)]
24. El-shafei, M.M.; Hamdy, A.; Hefny, M.M. Zero-valent iron nanostructures: Synthesis, characterization and application. *J. Environ. Biotechnol.* **2018**, *7*, 1–10.
25. Zhang, Z.; Ji, Y.; Li, J.; Zhong, Z.; Su, F. Synergistic effect in bimetallic copper-silver (CuAg) nanoparticles enhances silicon conversion in Rochow reaction. *RSC Adv.* **2015**, *5*, 54364–54371. [[CrossRef](#)]
26. Mahmoud, A.S.; Ismail, A.; Mostafa, M.K.; Mahmoud, M.S.; Ali, W.; Shawky, A.M. Isotherm and kinetic studies for heptachlor removal from aqueous solution using Fe/Cu nanoparticles, artificial intelligence, and regression analysis. *Sep. Sci. Technol.* **2020**, *55*, 684–696. [[CrossRef](#)]
27. Al-Namil, D.S.; El Khoury, E.; Patra, D. Solid-state green synthesis of Ag NPs: Higher temperature harvests larger Ag NPs but smaller size has better catalytic reduction reaction. *Sci. Rep.* **2019**, *9*, 1–9. [[CrossRef](#)] [[PubMed](#)]
28. Singh, J.; Chang, Y.Y.; Koduru, J.R.; Yang, J.K. Potential degradation of methylene blue (MB) by nano metallic particles: A kinetic study and possible mechanism of MB degradation. *Environ. Eng. Res.* **2018**, *23*, 1–9. [[CrossRef](#)]
29. Desalegn, B.; Megharaj, M.; Chen, Z.; Naidu, R. Green synthesis of zero valent iron nanoparticle using mango peel extract and surface characterization using XPS and GC-MS. *Heliyon* **2019**, *5*, e01750. [[CrossRef](#)]
30. Wang, J.; Liu, C.; Hussain, I.; Li, C.; Li, J.; Sun, X.; Shen, J.; Han, W.; Wang, L. Iron-copper bimetallic nanoparticles supported on hollow mesoporous silica spheres: The effect of Fe/Cu ratio on heterogeneous Fenton degradation of a dye. *RSC Adv.* **2016**, *6*, 54623–54635. [[CrossRef](#)]
31. Zhan, S.; Li, C.; Tian, H.; Ma, C.; Liu, H.; Luo, J.; Li, M. Synthesis, characterization and dye removal behavior of core-shell-shell Fe₃O₄/Ag/Polyoxometalates ternary nanocomposites. *Nanomaterials* **2019**, *9*, 1255. [[CrossRef](#)]
32. Miyama, T.; Yonezawa, Y. Photoinduced formation and aggregation of silver nanoparticles at the surface of carboxymethyl cellulose films. *J. Nano Res.* **2004**, *6*, 457–465. [[CrossRef](#)]
33. Han, L.; Xue, S.; Zhao, S.; Yan, Y.; Qian, L.; Chen, M. Biochar supported nanoscale iron particles for the efficient removal of methyl orange dye in aqueous solutions. *PLoS ONE* **2015**, *10*, e0132067. [[CrossRef](#)]
34. Luo, S.; Yang, S.; Wang, X.; Sun, C. Reductive degradation of tetrabromobisphenol A over iron-silver bimetallic nanoparticles under ultrasound radiation. *Chemosphere* **2010**, *79*, 672–678. [[CrossRef](#)]
35. Tengku Sallehudin, T.A.; Abu Seman, M.N.; Tuan Chik, S.M.S. Preparation and characterization silver nanoparticle embedded polyamide nanofiltration (NF) membrane. *MATEC Web Conf.* **2018**, *150*, 1–6. [[CrossRef](#)]
36. Akbari, B.; Tavandashi, M.P.; Zandrahimi, M. Particle size characterization of nanoparticles—A practical approach. *Iran. J. Mater. Sci. Eng.* **2011**, *8*, 48–56.
37. Wang, J.; Liu, C.; Li, J.; Luo, R.; Hu, X.; Sun, X.; Shen, J.; Han, W.; Wang, L. In-situ incorporation of iron-copper bimetallic particles in electrospun carbon nanofibers as an efficient Fenton catalyst. *Appl. Catal. B Environ.* **2017**, *207*, 316–325. [[CrossRef](#)]
38. Wang, J.; Liu, C.; Tong, L.; Li, J.; Luo, R.; Qi, J.; Li, Y.; Wang, L. Iron-copper bimetallic nanoparticles supported on hollow mesoporous silica spheres: An effective heterogeneous Fenton catalyst for orange II degradation. *RSC Adv.* **2015**, *5*, 69593–69605. [[CrossRef](#)]

39. Falicov, L.M.; Somorjai, G.A. Correlation between catalytic activity and bonding and coordination number of atoms and molecules on transition metal surfaces: Theory and experimental evidence. *Proc. Natl. Acad. Sci. USA* **1985**, *82*, 2207–2211. [[CrossRef](#)] [[PubMed](#)]
40. Huang, W.; Sun, G.; Cao, T. Surface chemistry of group IB metals and related oxides. *Chem. Soc. Rev.* **2017**, *46*, 1977–2000. [[CrossRef](#)]
41. Bond, G. Periodic variations in the catalytic properties of metals: The influence of solid state parameters on adsorption and catalysis. *Platin. Met. Rev.* **1968**, *12*, 100–105.
42. Ren, G.Q.; Pei, G.X.; Ren, Y.J.; Liu, K.P.; Chen, Z.Q.; Yang, J.Y.; Su, Y.; Liu, X.Y.; Li, W.Z.; Zhang, T. Effect of group IB metals on the dehydrogenation of propane to propylene over anti-sintering Pt/MgAl₂O₄. *J. Catal.* **2018**, *366*, 115–126. [[CrossRef](#)]
43. Ghanch, A.; Assi, H.A.; Baydoun, H.; Tuqan, A.M.; Bejjani, A. Fe₀-based trimetallic systems for the removal of aqueous diclofenac: Mechanism and kinetics. *Chem. Eng. J.* **2011**, *172*, 1033–1044. [[CrossRef](#)]
44. Zin, M.T.; Borja, J.; Hinode, H.; Kurniawan, W. Synthesis of Bimetallic Fe/Cu nanoparticles with different copper loading ratios. *Int. J. Chem. Nucl. Metall. Mater. Eng.* **2013**, *7*, 669–673.
45. Wang, T.; Su, J.; Jin, X.; Chen, Z.; Megharaj, M.; Naidu, R. Functional clay supported bimetallic nZVI/Pd nanoparticles used for removal of methyl orange from aqueous solution. *J. Hazard. Mater.* **2013**, *262*, 819–825. [[CrossRef](#)] [[PubMed](#)]
46. Hsieh, S.; Lin, P.Y. FePt nanoparticles as heterogeneous Fenton-like catalysts for hydrogen peroxide decomposition and the decolorization of methylene blue. *J. Nano Res.* **2012**, *14*, 956. [[CrossRef](#)]
47. Fathima, J.B.; Pugazhendhi, A.; Oves, M.; Venis, R. Synthesis of eco-friendly copper nanoparticles for augmentation of catalytic degradation of organic dyes. *J. Mol. Liq.* **2018**, *260*, 1–8. [[CrossRef](#)]
48. Li, P.; Song, Y.; Wang, S.; Tao, Z.; Yu, S.; Liu, Y. Enhanced decolorization of methyl orange using zero-valent copper nanoparticles under assistance of hydrodynamic cavitation. *Ultrason. Sonochem.* **2015**, *22*, 132–138. [[CrossRef](#)] [[PubMed](#)]
49. Devi, L.G.; Shyamala, R. Photocatalytic activity of SnO₂-a-Fe₂O₃ composite mixtures: Exploration of number of active sites, turnover number and turnover frequency. *Mater. Chem. Front.* **2018**, *2*, 796–806. [[CrossRef](#)]
50. Zhou, J.; Duan, X.; Ye, L.; Zheng, J.; Li, M.M.J.; Tsang, S.C.E.; Yuan, Y. Enhanced chemoselective hydrogenation of dimethyl oxalate to methyl glycolate over bimetallic Ag-Ni/SBA-15 catalysts. *Appl. Catal. A Gen.* **2015**, *505*, 344–353. [[CrossRef](#)]
51. Zhang, X.; Chen, S.; Wang, F.; Deng, L.; Ren, J.; Jiao, Z.; Zhou, G. Effect of surface composition and structure of the mesoporous Ni/KIT-6 catalyst on catalytic hydrodeoxygenation performance. *Catalysts* **2019**, *9*, 889. [[CrossRef](#)]
52. Bernard, P.; Stelmachowski, P.; Broś, P.; Makowski, W.; Kotarba, A. Demonstration of the influence of specific surface area on reaction rate in heterogeneous catalysis. *J. Chem. Educ.* **2021**, *98*, 935–940. [[CrossRef](#)]
53. Kondrat, S.S.; van Bokhoven, J.A. A perspective on counting catalytic active sites and rates of reaction using X-ray spectroscopy. *Top. Catal.* **2019**, *62*, 1218–1227. [[CrossRef](#)]
54. Weckhuysen, B.M. Determining the active site in a catalytic process: Operando spectroscopy is more than a buzzword. *Phys. Chem. Chem. Phys.* **2003**, *5*, 4351–4360. [[CrossRef](#)]
55. Valiyeva, G.G.; Bavasso, I.; Palma, L.D.; Hajiyeva, S.R.; Ramazanov, M.A.; Hajiyeva, F.V. Synthesis of Fe/Ni bimetallic nanoparticles and application to the catalytic removal of nitrates from water. *Nanomaterials* **2019**, *9*, 1130. [[CrossRef](#)]
56. Sui, C.; Xing, L.H.; Cai, X.; Wang, Y.; Zhou, Q.; Li, M. Co-supported CeO₂ nanoparticles for CO catalytic oxidation: Effects of different synthesis methods on catalytic performance. *Catalysts* **2020**, *10*, 243. [[CrossRef](#)]
57. Sarathy, V.; Tratnyek, P.G.; Nurmi, J.T.; Baer, D.R.; Amonette, J.E.; Chun, C.L.; Penn, R.L.; Reardon, E.J. Aging of iron nanoparticles in aqueous solution: Effects on structure and reactivity. *J. Phys. Chem. C* **2008**, *112*, 2286–2293. [[CrossRef](#)]
58. Shih, Y.H.; Tso, C.P.; Tung, L.Y. Rapid degradation of Methyl Orange with nanoscale zerovalent iron particles. *J. Environ. Eng. Manag.* **2010**, *20*, 137–143.
59. Chen, Z.X.; Jin, X.Y.; Chen, Z.; Megharaj, M.; Naidu, R. Removal of methyl orange from aqueous solution using bentonite-supported nanoscale zero-valent iron. *J. Colloid Interface Sci.* **2011**, *363*, 601–607. [[CrossRef](#)]
60. Shen, Z.; Liu, D.; Dong, X.; Shi, J.; Ma, Y.; Fan, J.; Zhang, L. Nitrate reduction using iron and copper bimetallic nanoparticles supported by chelating resin: Effect of solution chemistry, mechanism, and regeneration. *J. Environ. Eng.* **2020**, *146*, 04020011. [[CrossRef](#)]
61. Argyle, M.D.; Bartholomew, C.H. Heterogeneous catalyst deactivation and regeneration: A review. *Catalysts* **2015**, *5*, 145–269. [[CrossRef](#)]
62. Li, G.; Gao, S.; Zhang, G.; Zhang, X. Enhanced adsorption of phosphate from aqueous solution by nanostructured iron(III)-copper(II) binary oxides. *Chem. Eng. J.* **2014**, *235*, 124–131. [[CrossRef](#)]
63. Sharif, H.M.A.; Mahmood, A.; Cheng, H.Y.; Djellabi, R.; Ali, J.; Jiang, W.L.; Wang, S.S.; Haider, M.R.; Mahmood, N.; Wang, A.J. Fe₃O₄ nanoparticles coated with EDTA and Ag nanoparticles for the catalytic reduction of organic dyes from wastewater. *ACS Appl. Nano Mater.* **2019**, *2*, 5310–5319. [[CrossRef](#)]
64. Navalon, S.; Alvaro, M.; Garcia, H. Heterogeneous Fenton catalysts based on clays, silicas and zeolites. *Appl. Catal. B Environ.* **2010**, *99*, 1–26. [[CrossRef](#)]
65. Corbett, J.F. Pseudo first-order kinetics. *J. Chem. Educ.* **1972**, *49*, 663. [[CrossRef](#)]
66. Lin, Y.T.; Weng, C.H.; Chen, F.Y. Effective removal of AB24 dye by nano/micro-size zero-valent iron. *Sep. Purif. Technol.* **2008**, *64*, 26–30. [[CrossRef](#)]

67. Lai, B.; Chen, Z.; Zhou, Y.; Yang, P.; Wang, J.; Chen, Z. Removal of high concentration p-nitrophenol in aqueous solution by zero valent iron with ultrasonic irradiation (US-ZVI). *J. Hazard. Mater.* **2013**, *250–251*, 220–228. [[CrossRef](#)]
68. Herath, H.M.D.R.; Shaw, P.N.; Cabot, P.; Hewavitharana, A.K. Effect of ionization suppression by trace impurities in mobile phase water on the accuracy of quantification by high-performance liquid chromatography/mass spectrometry. *Rapid Commun. Mass Spectrom.* **2010**, *24*, 1502–1506. [[CrossRef](#)]
69. Waters Corporation US. Controlling Contamination in LC/MS Systems Best Practices. Available online: https://www.waters.com/webassets/cms/support/docs/715001307d_cntrl_cntm.pdf (accessed on 2 May 2020).
70. Xie, S.; Huang, P.; Kruzic, J.J.; Zeng, X.; Qian, H. A highly efficient degradation mechanism of methyl orange using Fe-based metallic glass powders. *Sci. Rep.* **2016**, *6*, 21947. [[CrossRef](#)]
71. Sarvari, H.; Goharshadi, E.K.; Samiee, S.; Ashraf, N. Removal of methyl orange from aqueous solutions by ferromagnetic Fe/Ni nanoparticles. *Phys. Chem. Res.* **2018**, *6*, 433–446.
72. Lai, B.; Ji, Q.; Yuan, Y.; Yuan, D.; Zhou, Y.; Wang, J. Degradation of ultrahigh concentration pollutant by Fe/Cu bimetallic system at high operating temperature. *Korean J. Chem. Eng.* **2016**, *33*, 207–215. [[CrossRef](#)]
73. Shafi, P.M.; Bose, A.C. Impact of crystalline defects and size on X-ray line broadening: A phenomenological approach for tetragonal SnO₂ nanocrystals. *AIP Adv.* **2015**, *5*, 057137. [[CrossRef](#)]